Biosensors and Bioelectronics 126 (2019) 23–29

Contents lists available at ScienceDirect

Biosensors and Bioelectronics

journal homepage: www.elsevier.com/locate/bios

Label-free photoelectrochemical immunosensor for amyloid β-protein detection based on $SnO_2/CdCO_3/CdS$ synthesized by one-pot method

Yifeng Zhang, Mengdi Wang, Yaoguang Wang*, Jinhui Feng, Yong Zhang, Xu Sun, Bin Du, Qin Wei*

Key Laboratory of Interfacial Reaction & Sensing Analysis in Universities of Shandong, School of Chemistry and Chemical Engineering, University of Jinan, Jinan 250022, PR China

ARTICLE INFO

Keywords:
Photoelectrochemical immunosensor
Amyloid β-protein
One-pot method
$SnO_2/CdCO_3/CdS$ nanocomposite

ABSTRACT

In this study, we propose a $SnO_2/CdCO_3/CdS$-based label-free photoelectrochemical (PEC) immunosensor for the sensitive quantification of amyloid β-protein (Aβ) which plays a critical role in the early diagnosis of Alzheimer's disease. Under specific pH conditions, $SnO_2/CdCO_3/CdS$ was first designed and successfully synthesized with simple one-pot method. The synthesis of $SnO_2/CdCO_3/CdS$ circumvents the trouble of traditional composite materials to be gradually compounded, saving a lot of time and energy. The synthesis mechanism of $SnO_2/CdCO_3/CdS$ nanocomposite was also deeply explored. Moreover, thanks to the matched energy levels of its three components, $SnO_2/CdCO_3/CdS$ nanocomposite exhibited enhanced photocurrent intensity, which is dozens of times bigger than any of its components, thus making it an excellent photoactive matrix for PEC immunosensor. Under optimal conditions, the as-constructed PEC immunosensor manifested a broad linear range (0.1 pg mL^{-1} to 100 ng mL^{-1}) with a low detection limit (LOD, 0.05 pg mL^{-1}, S/N = 3). High selectivity, coupled with good stability, allowed the developed PEC immunosensor to be applied in the clinical detection of Aβ or other biomarkers in human serum.

1. Introduction

Amyloid β-protein (Aβ), a polypeptide containing 39–43 amino acids, is known as the reason of neuronal death and is widely recognized as a biomarker of Alzheimer's disease (AD) (Flammang et al., 2012; Wang et al., 2018a). Its content is closely related to the development of the disease (Economou et al., 2016). Therefore, accurate detection of Aβ is significant for the timely diagnosis and treatment of the disease (Wang et al., 2016). Over the last several years, strenuous efforts have been made in biomarker detection similar to Aβ (Li et al., 2017; Liu et al., 2016; Ren et al., 2017; X. Wang et al., 2017; Wang et al. 2018b; L. Yang et al., 2017). Among the various detection methods which have been developed, photoelectrochemical (PEC) immunoassay has triggered off increasing attention in the field of biological analysis because it integrates many merits encompassing low background signal, high selectivity, rapid detection and good stability (Feng et al., 2018b; Zang et al., 2017; Zhao et al., 2017). As the important factors of the PEC immunosensor, materials with high photosensitivity and stability have always been the pursuit of researchers (Shangguan et al., 2015; Shi et al., 2018). TiO_2, WO_3, BiOI and a series of traditional materials have been exploited as photoactive matrix after being doped or sensitized (Q. Han et al., 2018; Liu et al., 2017; X. Yang et al., 2017). Nevertheless, as far as we know, there are very few reports about the application of SnO_2 and $CdCO_3$ in the PEC immunosensor. Herein, $SnO_2/CdCO_3/CdS$ nanocomposite was first synthesized and employed as photoactive matrix for PEC immunosensor.

Stannic oxide (SnO_2), a n-type semiconductor, has an extensive use in many fields such as gas sensor (Chesler et al., 2016), solar cells (Dong et al., 2014) and photocatalysis (Niu et al., 2010) due to its high electron mobility and good chemical stability. However, SnO_2 suffers from the broad band gap (~3.6 eV) which makes it produce negligible photocurrent response in visible light, seriously hindering its application in PEC immunoassay (H. Han et al., 2018). In order to promote the PEC performance of SnO_2, some methods of compounding or doping have been conducted (Dou et al., 2011; Guo et al., 2013; Zhang et al., 2016). Interestingly, it is found that compounding with other semiconductors to form heterojunction is the most successful approach (Pan et al., 2013; Sheridan et al., 2017). Once the heterojunction is formed, the built-in electric field will promote the transfer of photo-induced charge to achieve the unity of Fermi level, which inhibits the recombination of the electron-hole pairs, making an increment in photocurrent response (Fan et al., 2016; Y. Wang et al., 2017).

* Corresponding authors.
E-mail addresses: wangyaoguang9002@163.com (Y. Wang), sdjndxwq@163.com (Q. Wei).

https://doi.org/10.1016/j.bios.2018.10.045
Received 27 July 2018; Received in revised form 20 October 2018; Accepted 22 October 2018
Available online 24 October 2018

$CdCO_3$, an indirect-band-gap semiconductor with the adjustable energy gap, has been widely employed in stabilizers, additives and catalysis on account of its several important physicochemical properties (Vidyasagar et al., 2018). CdS, a n-type semiconductor with suitable bandgap, is deemed an ideal candidate compound to enhance the PEC performance of general material (Feng et al., 2018a; Xu et al., 2015) and it has an extensive application in photocatalysis (Zheng and Wang, 2015) and photodegratation (Moualkia et al., 2017). Given the above, $CdCO_3$ and CdS were selected to combine with SnO_2 to improve the PEC performance of SnO_2. However, compounding is often accompanied by tedious procedures. For instance, Liu and co-workers synthesized core-shell-structure CdS@SnO_2 by ultrasonically mixing pre-prepared CdS and SnO_2 (Liu et al., 2015). The as-synthesized CdS@SnO_2 takes on higher photocatalytic activity than that of pure SnO_2. But its synthesis involves three tedious steps (synthesis of CdS, synthesis of SnO_2, and ultrasonic mixing of the two materials) which we have always wanted to avoid. Further, Zhang and co-workers found that hydrothermally synthesized SnS_2/SnO_2 (H-SnS_2/SnO_2) exhibits better photocatalytic performance than that of physically mixed SnS_2/SnO_2 (PM-SnS_2/SnO_2) (Y.C. Zhang et al., 2014). They clarified that if not be combined so tightly, the components of PM-SnS_2/SnO_2 would tend to separate when immersed in aqueous solution. By contrast, H-SnS_2/SnO_2 possesses a more firm contact, which assures a tight heterointerface and causes the reduction of the dissociation of composite, promoting effectively the charge separation and transfer. Given the above, $SnO_2/CdCO_3/CdS$ nanocomposite material was synthesized with one-step hydrothermal method under alkaline conditions in this study.

Through a string of researches, we found that SnS_2 could not be hydrothermally produced under alkaline conditions even with the presence of S^{2-}, and the final product obtained was SnO_2. Moreover, S^{2-} and CO_3^{2-} hydrolyzed by thiourea in heated aqueous solution, coupled with Cd^{2+}, would produce $CdCO_3$/CdS nanocomposite. In view of these facts, $SnO_2/CdCO_3/CdS$ nanocomposite with excellent photocurrent response was synthesized with one-step hydrothermal method under alkaline conditions. What's more, by controlling the feed ratios of the Sn source and Cd source, composition-tunable $SnO_2/CdCO_3/CdS$ nanocomposite was obtained and the one with the largest photocurrent response was employed as photoactive matrix to construct a label-free PEC immunosensor for Aβ detection (Scheme 1). After being modified with $SnO_2/CdCO_3/CdS$ nanocomposite, the ITO electrode was immersed in an aqueous solution of thioglycolic acid. The functionalization of $SnO_2/CdCO_3/CdS$ by thioglycolic acid introduced the carboxyl groups, which could bind to the anti-Aβ after EDC/NHS activation. Subsequently, the modified electrodes were incubated with the Aβ of different concentrations to generate immune complexes after blocking the active sites with BSA. Aβ and anti-Aβ produces immune complexes, whose excellent insulation and high mass transfer resistance make the detected photocurrent reduce along with the increasing of Aβ. In order to obtain a larger and more stable output signal-photocurrent, ascorbic acid (AA) was introduced to trap photo-induced holes and prevent the photo-corrosion of CdS. The as-fabricated PEC immunosensor exhibits satisfactory performance in detecting Aβ in the actual sample, which opens up a new platform for the detection of other biomarkers.

2. Experimental section

2.1. Chemicals and instruments

$SnCl_4{\cdot}5H_2O$ (CAS: 10026-06-9) and thiocarbamide (CAS: 62-56-6) were obtained from Macklin Biochemical Co., Ltd (Shanghai, China). The details are shown in Supplementary Material.

2.2. Preparation of nanomaterials

$SnO_2/CdCO_3/CdS$ was synthesized by a simple one-step hydrothermal route. Typically, 2.4 mmol $SnCl_4{\cdot}5H_2O$, 0.6 mmol $CdCl_2{\cdot}2.5H_2O$ and excess thiocarbamide (6 mmol) were thoroughly dissolved in 34 mL ultrapure water. The above solution was transferred into a 50 mL Teflon-lined autoclave under the condition that its pH was adjusted to 10 by concentrated ammonia. It is worth mentioning that during the pH adjustment process, the solution changed from clarification to a sol-like white uniform substance. Orange-yellow precipitate was obtained after the autoclave was maintained at 180 °C for 12 h. Then the as-obtained precipitate was washed with ultrapure water and ethanol several times in turn. At last, the product was dried at 60 °C overnight in vacuum condition for future use. In addition, for comparison, SnO_2 and $CdCO_3$/CdS were prepared with the same method in the absence of Cd or Sn sources.

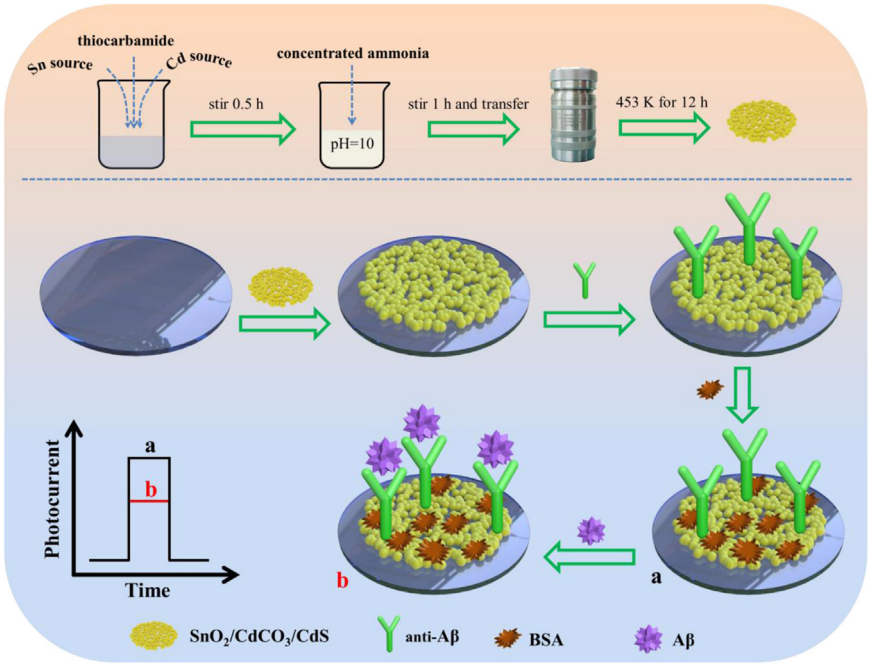

Scheme 1. Schematic illustration for the preparation of $SnO_2/CdCO_3/CdS$ and the fabrication of PEC immunosensor.

2.3. Construction of PEC immunosensor

Before it came into use, ITO glass was cut into rectangular pieces with the size of 2.5 cm × 1 cm, then these slices were respectively sonicated for 30 min in the following solutions: ultrapure water, acetone, ultrapure water, ethanol, ultrapure water and NaOH solution (1 mol L^{-1}) in turn. Finally, they were rinsed thoroughly with ultrapure water and dried in drying oven. After their effective sensing areas (modified areas) were controlled to 12.5 mm^2 by the adhesive sticker (See Fig. S1A for details), the clean slices would be ready for modification. Scheme 1 reveals the construction process of PEC immunosensor. Concretely, the ITO electrode was firstly furnished with 8 μL $SnO_2/CdCO_3/CdS$ solution (3 mg mL^{-1}) and dried at room temperature. After being soaked in mercaptoacetic acid solution (3 mmol L^{-1}) at room temperature for 30 min, the modified electrode was incubated at 4 °C for 4 h to bond with anti-Aβ through classical coupling reaction between carbonyl groups of TGA and amino groups of anti-Aβ with the help of 6 μL EDC/NHS solution (5 mmol L^{-1} of EDC, 1 mmol L^{-1} of NHS). Next, the modified electrode was incubated with 6 μL bovine serum albumin (BSA) solution (0.1 wt%) at 37 °C for 1 h to block nonspecific binding sites. Subsequently, 6 μL Aβ solutions with different concentrations were dropped on diverse electrodes. The as-obtained electrode was ready for photocurrent test after being washed with PBS.

2.4. PEC measurement procedure

The modified electrodes were investigated in quartz electrolyser with 10 mL PBS (pH 7.4) containing 0.2 mol L^{-1} AA in drawing the work curve. The photocurrent response was recorded by a PEC workstation at 0 V bias voltage under the irradiation of light (450 nm, 140 W/m^2) switched on/off every 20 s.

3. Result and discussion

3.1. Characterization of applied materials

Fig. 1A exhibits the XRD patterns of as-prepared nanomaterials. By comparing curve a, b with curve c, it is easy to find that curve c almost contains all the major peaks of curve a and b, which means that the as-synthesized $CdCO_3/CdS$ is made up of $CdCO_3$ (JCPDS: 42–1342) and CdS (JCPDS: 41–1049). What's more, the element mapping for the TEM image of $CdCO_3/CdS$ (Fig. S2) further confirms the existence of these four elements-Cd, C, O and S. The as-synthesized SnO_2 presents the diffraction peaks at 26.61°, 33.89°, 37.95° and 51.78°, which corresponds to (110), (101), (200) and (211) lattice planes of tetragonal SnO_2 (JCPDS: 41–1445). In addition, most of the diffraction peaks of SnO_2 could be clearly identified in the $SnO_2/CdCO_3/CdS$ while no obvious diffraction peaks of $CdCO_3$ or CdS could be clearly recognized in the composites on account of the superposition of the diffraction peaks at the same position and the low contents of $CdCO_3$ and CdS. As can be seen in Fig. 1B, SnO_2 (curve a) has weak absorption in the visible region while $CdCO_3/CdS$ (curve b) exhibits strong light absorption. Although $SnO_2/CdCO_3/CdS$ is weaker than $CdCO_3/CdS$ in light absorption, it shows a stronger photocurrent response, proving that the photogenerated charge carriers of $SnO_2/CdCO_3/CdS$ are utilized more effectively. The structures of synthesized nanomaterials were characterized by High-resolution Transmission Electron Microscopy (HRTEM). The as-synthesized $CdCO_3/CdS$ (Fig. 1D) presents rod-like nanostructures with lengths from 60 to 120 nm, while SnO_2 (Fig. 1C) and $SnO_2/CdCO_3/CdS$ (Fig. 1E) exhibit a spot shape with a uniform size about 5 nm. Fig. 1F reveals that the three components of $SnO_2/CdCO_3/CdS$ are closely connected. $SnO_2/CdCO_3/CdS$ nanocomposite was also subjected to X-ray photoelectron spectroscopy (XPS) (Fig. S3) and energy dispersive X-ray spectrum (EDS) (Fig. S4) to confirm the existence and content of O, Sn, Cd, C and S. The XPS spectrum of $SnO_2/CdCO_3/CdS$ (Fig. S3B) reveals a strong peak at 530.85 eV corresponding to the

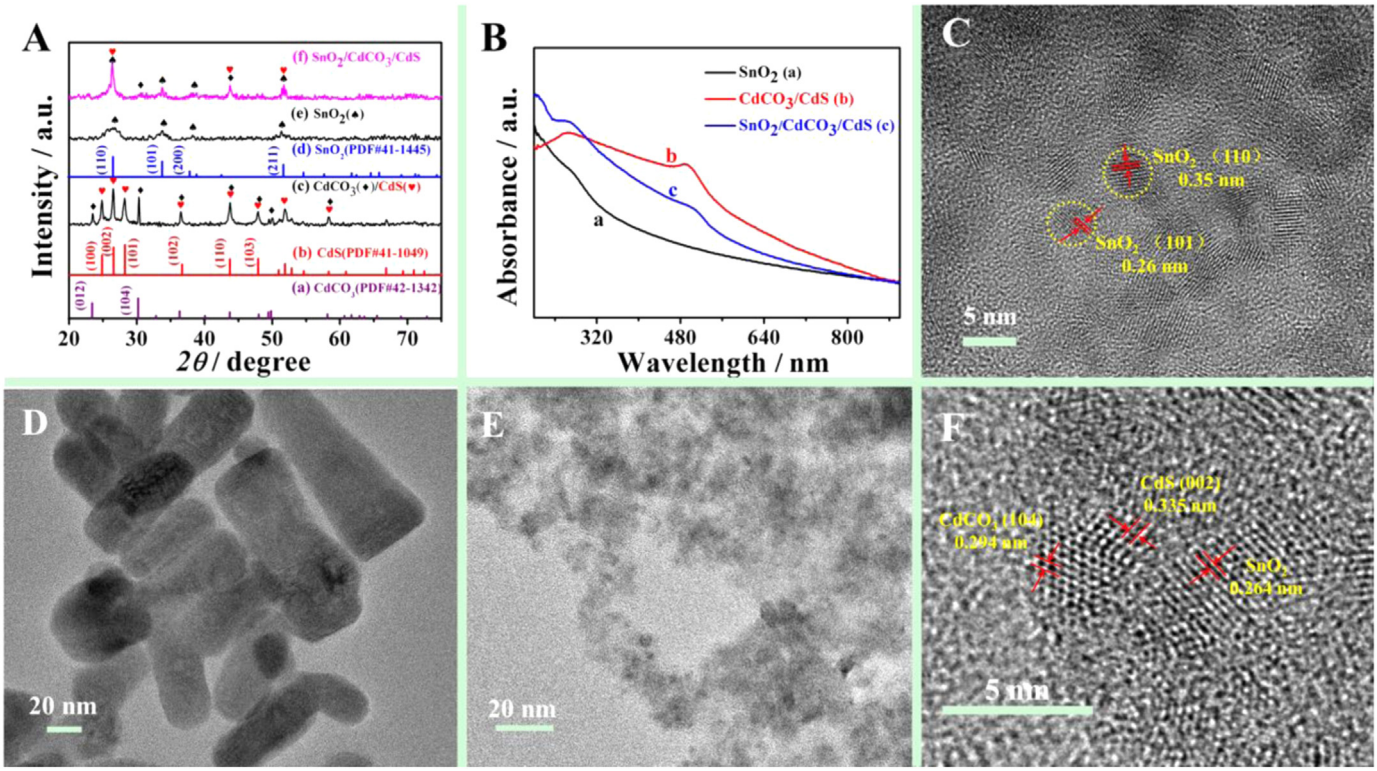

Fig. 1. (A) XRD patterns of the as-prepared materials. (B) UV–vis absorption spectra for the as-prepared materials. TEM images of (C) SnO_2, (D) $CdCO_3/CdS$, (E) and (F) $SnO_2/CdCO_3/CdS$ with different scales.

binding energy of O^{2-} 1 s. Compared with normal Sn^{4+}, the two peaks (Fig. S3C) at 495.35 eV and 486.95 eV, corresponding to the binding energy of Sn^{4+} $3d_{3/2}$ and Sn $3d_{5/2}$ in SnO_2, shift toward higher energy zone due to a possible Fermi energy level movement caused by the close interaction between SnO_2 and $CdCO_3$/CdS nanocomposite (Stranick and Moskwa, 1993; Zhang et al., 2017). On the contrary, the two peaks (Fig. S3D) originated from the binding energy of Cd 3d (411.85 eV for Cd $3d_{3/2}$ and 405.25 eV for Cd $3d_{5/2}$) shift slightly toward lower energy zone as compared to literature (Tkachenko et al., 1993). In Fig. S3F, the peaks at 162.4 eV and 161.25 eV corresponding to the binding energy of S^{2-} $2p_{1/2}$ and S^{2-} $2p_{3/2}$ in CdS shift toward lower energy zone in comparison with literature (Li et al., 2015). Fig. S3E demonstrates three peaks at 288.7 eV, 286.4 eV and 284.9 eV which correspond to C^{4+} 1s. We can further see the content ratio of the five elements of Sn, Cd, S, C and O in the EDS image (Fig. S4). It can be deduced from the atomic ratio of Sn, Cd and S that the ratio of SnO_2, $CdCO_3$ and CdS is 68.7: 0.6: 30.7. The extra C and O is likely to be derived from carbon conductive adhesive or adsorbed air. Hence, the possible molar ratio of SnO_2, $CdCO_3$ and CdS is 68.7: 0.6: 30.7.

3.2. Mechanism discussion

In the proposed one-pot hydrothermal synthesis of SnO_2/$CdCO_3$/CdS nanocomposite, $SnCl_4{\cdot}5H_2O$ and $CdCl_2{\cdot}2.5H_2O$ could dissolve in H_2O and release Sn^{4+} (Eq. (1)) and Cd^{2+} (Eq. (2)). Thiocarbamide would produce H_2S and CO_2 (Eq. (3)) during hydrolysis at high temperature under alkaline conditions, followed by the reaction of CO_2 with OH^- to yield CO_3^{2-} (Eq. (4)). As a result, CO_3^{2-} would react with Cd^{2+} to generate $CdCO_3$ (Eq. (5)) and H_2S would react with Cd^{2+} to yield CdS (Eq. (6)). Simultaneously, Sn^{4+} would react with OH^- to produce $Sn(OH)_4$ (Eq. (7)) which could be further dehydrated to create SnO_2 (Eq. (8)). Thus, when the three source materials are all involved in the reaction, SnO_2/$CdCO_3$/CdS nanocomposite can be generated and the proportion of SnO_2 can be adjusted by adding Sn source with different doses. When $CdCl_2{\cdot}2.5H_2O$ is not added, the reactions of Eqs. (2), (5) and (6) would not occur and the reaction product is just SnO_2 which is consistent with the results obtained by XRD characterization. And in the absence of $SnCl_4{\cdot}5H_2O$, the reactions of Eqs. (1), (7) and (8) cannot take place and the product is just $CdCO_3$/CdS nanocomposite corresponding to the characterization result of XRD. What's more, when Cd source and Sn source are added all at once, Eqs. (7) and (8) take precedence over Eqs. (5) and (6). Numerous preferentially-generated SnO_2 particles act as the support for the growth of CdS and $CdCO_3$, which interrupts their self-growth so that only small-sized particles can be obtained.

$$SnCl_4{\cdot}5H_2O \rightarrow Sn^{4+} + 4Cl^- + 5H_2O \quad (1)$$

$$CdCl_2.2{\cdot}5H_2O \rightarrow Cd^{2+} + 2Cl^- + 2{\cdot}5H_2O \quad (2)$$

$$CS(NH_2)_2 + 2H_2O \rightarrow CO_2 + 2NH_3 + H_2S \quad (3)$$

$$CO_2 + 2OH^- \rightarrow CO_3^{2-} + H_2O \quad (4)$$

$$Cd^{2+} + CO_3^{2-} \rightarrow CdCO_3 \quad (5)$$

$$H_2S + Cd^{2+} + 2OH^- \rightarrow CdS + 2H_2O \quad (6)$$

$$Sn^{4+} + 4OH^- \rightarrow Sn(OH)_4 \quad (7)$$

$$Sn(OH)_4 \rightarrow SnO_2 + 2H_2O \quad (8)$$

Fig. 2A shows the results of the photocurrent response test of different materials in PBS (pH = 7.4) dissolving 0.1 mol L^{-1} AA. The electrode modified with SnO_2/$CdCO_3$/CdS possesses the maximum photocurrent intensity among the three tested electrodes which is 80 times that of SnO_2 and 6 times that of $CdCO_3$/CdS. According to the energy band theory, combined with experimental results, the mechanism of charge transfer for PEC signal amplification of SnO_2/$CdCO_3$/CdS was inferred as shown in Fig. 2B. The conduction band edge potentials for SnO_2, $CdCO_3$ and CdS were estimated to be 0, −0.66, and −0.7 eV which are roughly ladder-like distribution (Guo et al., 2014; Vidyasagar et al., 2018). As a result, the photo-induced electrons can be transferred quickly from the CB of CdS to the CB of $CdCO_3$ and finally to the CB of SnO_2, which greatly depress the recombination rate of photo-induced electron-hole pairs. Additionally, the work function of ITO is −5 eV, lower than the CB of SnO_2, which would further promote the transfer of electrons to the electrode and result in larger photocurrent (X. Zhang et al., 2014). In this way, the electrode modified with SnO_2/$CdCO_3$/CdS nanocomposite possesses the maximum photocurrent response among the three tested materials (SnO_2, $CdCO_3$/CdS and SnO_2/$CdCO_3$/CdS). It is noteworthy that the SnO_2/$CdCO_3$/CdS nanocomposite prepared by the one-pot synthesis method also takes on 5-fold photocurrent in comparison with the nanocomposite prepared by sequent modification, which proves that the one-pot synthetic SnO_2/$CdCO_3$/CdS exhibits stronger interfacial connection and better performance. At the same time, ascorbic acid (AA), a chemical that was extremely easy to give electrons and was oxidized, was introduced to trap photo-induced holes to further reduce charge recombination rate, which also protected CdS from photo-corrosion.

3.3. Characterization of the as-perpared PEC immunosensor

Electrochemical impedance spectroscopy (EIS) and photocurrent-time test were carried out to analyze the stepwise assembly process of the PEC immunosensor. EIS was measured by employing $[Fe(CN)_6]^{3-/4-}$ (5 mmol L^{-1}) as redox probe in 10 mL of KCl solution (0.1 mol L^{-1}) at a frequency of 10^{-1}–10^5 Hz with AC amplitude 5 mV. As is demonstrated

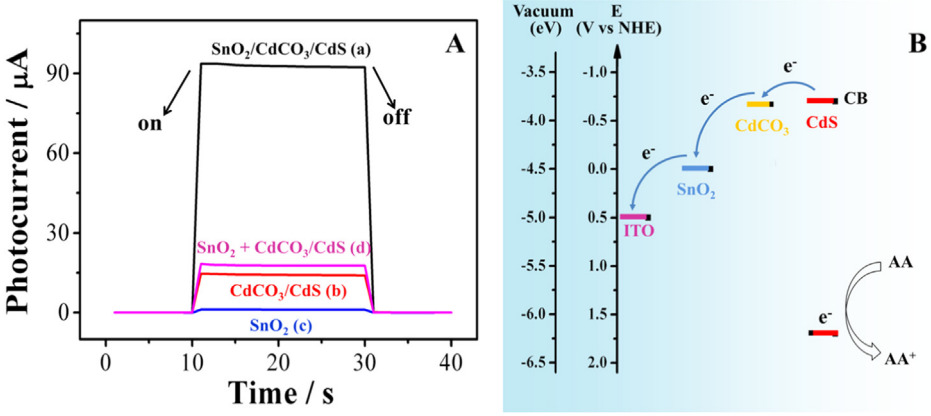

Fig. 2. (A) Photocurrent of electrode (a) ITO-SnO_2/$CdCO_3$/CdS, (b) ITO-$CdCO_3$/CdS, (c) ITO-SnO_2, (d) ITO-SnO_2-$CdCO_3$/CdS (0.1 mol L^{-1} AA, pH = 7.4); (B) Possible charge transfer mechanism of ITO-SnO_2/$CdCO_3$/CdS.

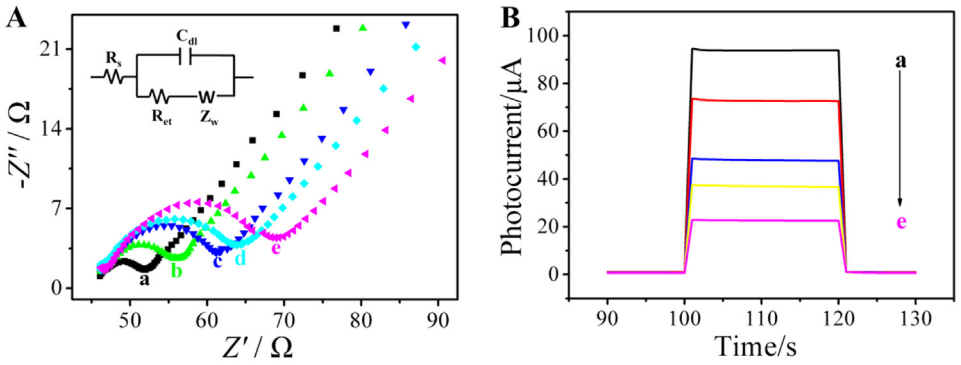

Fig. 3. (A) Nyquist plots of EIS and (B) photocurrent responses in the different stages of the electrode modification: (a) $SnO_2/CdCO_3/CdS$, (b) $SnO_2/CdCO_3/CdS$/(EDC/NHS), (c) $SnO_2/CdCO_3/CdS$/(EDC/NHS)/anti-Aβ, (d) $SnO_2/CdCO_3/CdS$/(EDC/NHS)/anti-Aβ/BSA, (e) $SnO_2/CdCO_3/CdS$/(EDC/NHS)/anti-Aβ/BSA/Aβ.

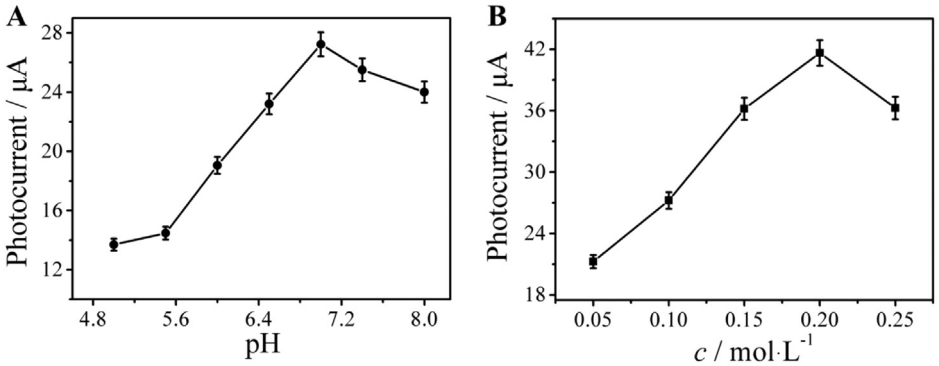

Fig. 4. The effect of (A) pH of electrolyte solution and (B) AA concentration on photocurrent response. $c_{Aβ}$ = 500 pg mL^{-1}, Error bars = SD (n = 3).

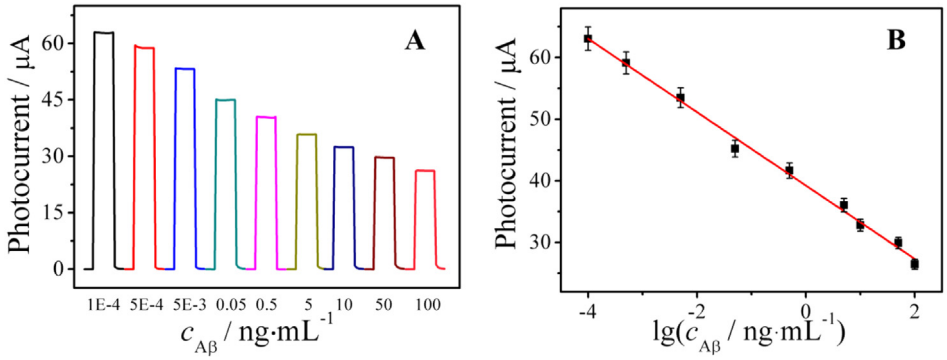

Fig. 5. (A) Photocurrent response of the immunosensor toward different concentrations of Aβ. (B) Calibration curve of the immunosensor for Aβ detection.

in Fig. 3A, after the modification of $SnO_2/CdCO_3/CdS$ nanocomposite on ITO electrode, a small semicircle (curve a) representing the electron transfer resistance (R_{et}) appeared in the Nyquist plot of EIS which indicates a diffusional limiting step of the electrodes. Then the drop of EDC/NHS, which can promote the amidation between -COOH group of TGA and -NH_2 of anti-Aβ, caused a minor change (curve b) in R_{et}, suggesting the successful modification. With the successive decoration of anti-Aβ (curve c), BSA (curve d) and Aβ (curve e), the R_{et} values were getting bigger and bigger due to their insulation property, indicating their successful immobilization on the electrode. The equivalent circuit of the EIS simulated with ZSimpWin software is embedded in Fig. 1A and the values of R_s, R_{et}, C_{dl} and Z_W are shown in Table S1. Meanwhile, the photocurrent-time test was implemented in PBS (pH = 7.4) containing 0.1 mol L^{-1} AA to monitor the change of photocurrent in each step of the construction process (Fig. 3B). The electrode modified with $SnO_2/CdCO_3/CdS$ possesses the highest photocurrent about 94 μA (curve a) which is crucial for the photoactive matrix of PEC sensor. When the classic amidation reagent-EDC/NHS was attached on the electrode, the photocurrent declined to about 73 μA (curve b). Subsequently, the value of photocurrent continued to decline after the assemblies of anti-Aβ (curve c) and BSA (curve d) in that they impeded the diffusion of AA to the surface of the electrode. After the Aβ was added, the anti-Aβ on the surface of the modified electrode would react with it specifically to form an immune complex which takes on big stereospecific blockade and further decreased the photocurrent (curve e). The changes in photocurrent value of the electrodes at different stages of modification further verified the successful construction of the PEC immunosensor.

3.4. Optimization of photoactive matrix and test conditions

In this study, the photocurrent responses of the synthesized

materials with different proportions of Sn and Cd source were tested and the specific addition amount and the corresponding photocurrent are shown in Table S2. It can be seen from it that the composite-c (Sn: Cd = 4:1) possesses the largest photocurrent response and it was selected to characterize and fabricate PEC immunosensor.

The effect of pH on the photocurrent response of the as-fabricated PEC immunosensor was studied in PBS containing 0.1 mol L^{-1} AA within the range of 5–8 pH value (Fig. 4A). The PEC immunosensor shows the maximum photocurrent value when pH is 7. Given this, 7 was chosen as the optimal pH value for the later photocurrent response test.

As we all know, the photo-induced electron-hole pairs are very easy to recombine, which is very detrimental to the generation of photocurrent. Thus, AA was employed as the hole-traping dopant to hinder the recombination of electron-hole pairs. And the effects of the concentration of AA on the photocurrent response are shown in Fig. 4B. The photocurrent value reaches peak point when the concentration of AA is 0.2 mol L^{-1}. 0.2 mol L^{-1} was therefore regarded as the optimal concentration of AA for subsequent tests. Similarly, the photocurrent action spectra of $SnO_2/CdCO_3/CdS$ nanocomposite were also tested and the results are shown in Fig. S5. We can see from it that the larger the wavelength of the excitation light, the smaller the photocurrent response. But taking into account the softness of the light, 450 nm was chosen as the optimal wavelength for the excitation light.

3.5. PEC analysis of Aβ

To evaluate the analytical performance of the as-fabricated PEC immunosensor, the photocurrent-time test was carried out on a series of electrodes modified by Aβ with different concentrations under optimal experimental conditions and the data are presented in Fig. 5A. The 10-based logarithm value of concentration of the Aβ and the photocurrent show a linear relationship from 0.1 pg mL^{-1} to 100 ng mL^{-1} with a detection limit of 50 fg mL^{-1} (S/N = 3). The calculated linear relational expression is $I = -5.954 \lg(c) + 39.22$ whose correlation coefficient is 0.994 (Fig. 5A). Compared with some previously reported methods for Aβ detection, the proposed PEC immunosensor shows a wider linear range and a higher sensitivity (Table S3). The test results indicate that the as-fabricated PEC immunosensor takes on excellent potential for rapid and sensitive detection of Aβ or other biomarkers.

3.6. Repeatability, selectivity, stability of the proposed PEC immunosensor

To explore the repeatability of the PEC immunosensor, five identical electrodes modified with Aβ (500 pg mL^{-1}) were employed for repetitive experiment under the same condition and the calculated relative standard deviation (RSD) is 3.0%. Simultaneously, samples consisting of 50 pg mL^{-1} Aβ and 5 ng mL^{-1} interfering substances (prostatic specific antigen (PSA), insulin and alpha fetoprotein (AFP)) were chosen to characterize the selective performance of the PEC immunosensor. As is seen from Fig. S6A, the interferents contained in the samples bring about minor change in photocurrent response, which is acceptable (RSD = 1.4%) and indicates an excellent selectivity of the proposed PEC immunosensor. What's more, stability is a rigid index of the immunosensor and it was evaluated in this work. The excitation light source circulates at a frequency in which it switches on and off at 20-second intervals for 10 cycles and the results are presented in Fig. S6B. It can be seen from the figure that there is no significant undulation in photocurrent and the calculated RSD is 0.79% (n = 10), suggesting a satisfactory stability. Besides, the storage stability of the proposed biosensor was also evaluated with Aβ at a concentration of 500 pg mL^{-1} and the results are shown in Fig. S7. After 15 days of storage (4 °C, out of light), the measured current value dropped to 36.4 μA, accounting for 92% of the photocurrent on the first day, which indicated its satisfactory storage stability.

3.7. Preliminary application in actual samples

In order to evaluate feasibility of the as-fabricated PEC immunosensor, the recovery experiment was conducted via detecting Aβ in serum samples. After being diluted, the serum samples were mixed with standard Aβ solution in different concentrations for detection. As is depicted in Table S4, the recovery fell between 98.9% and 101%, which indicated the proposed PEC immunosensor possesses excellent potentiality for Aβ detection in real biological samples.

4. Conclusion

In summary, a novel label-free PEC immunosensor was proposed for Aβ detection with $SnO_2/CdCO_3/CdS$ nanocomposite as its signal indicator. $SnO_2/CdCO_3/CdS$ nanocomposite, which was ingeniously designed and successfully synthesized with one-pot method, takes on nearly 80-fold bigger photocurrent response than that of SnO_2 and 6-fold higher than $CdCO_3/CdS$ due to the good synergistic effect of its three components. Benefiting from the excellent photocurrent response of the nanocomposite, a wide linear range from 0.1 pg mL^{-1} to 100 ng mL^{-1} with the detection limit of 50 fg mL^{-1} were obtained. Meanwhile, rapid detection, high selectivity and good stability were also well exhibited by the simple PEC immunosensor. In view of these results, the developed PEC immunosensor not only enlarges the design space of PEC studies, but it also provides a promising platform for clinical diagnosis and human health monitoring. However, the photoactive matrix synthesized in this work require further processing to have better biocompatibility, which complicate the construction of immunosensor. Therefore, the development of photoactive materials with high biocompatibility remain the goal of researchers to further improve the performance and convenience of sensors.

Acknowledgement

This study was supported by the National Natural Science Foundation of China (Nos. 21575050, 21627809, 21777056, 21775053), the Natural Science Foundation of Shandong Province (No. ZR2017MB027) and QW thanks the Special Foundation for Taishan Scholar Professorship of Shandong Province (No. ts20130937) and UJN.

Appendix A. Supporting information

Supplementary data associated with this article can be found in the online version at doi:10.1016/j.bios.2018.10.045.

References

Chesler, P., Hornoiu, C., Mihaiu, S., Vladut, C., Moreno, J.M.C., Anastasescu, M., Moldovan, C., Firtat, B., Brasoveanu, C., Muscalu, G., 2016. Beilstein J. Nanotech. 7, 2045–2056.
Dong, Z., Ren, H., Hessel, C.M., Wang, J., Yu, R., Jin, Q., Yang, M., Hu, Z., Chen, Y., Tang, Z., 2014. Adv. Mater. 26, 905–909.
Dou, X., Sabba, D., Mathews, N., Wong, L.H., Lam, Y.M., Mhaisalkar, S., 2011. Chem. Mater. 23, 3938–3945.
Economou, N.J., Giammona, M.J., Do, T.D., Zheng, X., Teplow, D.B., Buratto, S.K., Bowers, M.T., 2016. J. Am. Chem. Soc. 138, 1772–1775.
Fan, G.-C., Zhu, H., Du, D., Zhang, J.-R., Zhu, J.-J., Lin, Y., 2016. Anal. Chem. 88, 3392–3399.
Feng, J., Li, F., Li, X., Wang, Y., Fan, D., Du, B., Li, Y., Wei, Q., 2018a. Biosens. Bioelectron. 117, 773–780.
Feng, J., Li, Y., Gao, Z., Lv, H., Zhang, X., Dong, Y., Wang, P., Fan, D., Wei, Q., 2018b. Sens. Actuat. B-Chem. 270, 104–111.
Flammang, B., Pardossi-Piquard, R., Sevalle, J., Debayle, D., Dabert-Gay, A.-S., Thévenet, A., Lauritzen, I., Checler, F., 2012. J. Alzheimer's Dis. 30, 145–153.
Guo, C.X., Dong, Y., Yang, H.B., Li, C.M., 2013. Adv. Energy Mater. 3, 997–1003.
Guo, S., Li, D., Zhang, Y., Zhang, Y., Zhou, X., 2014. Electrochim. Acta 121, 352–360.
Han, H., Kment, S., Karlicky, F., Wang, L., Naldoni, A., Schmuki, P., Zboril, R., 2018a. Small 14, 1703860.
Han, Q., Wang, R., Xing, B., Zhang, T., Khan, M.S., Wu, D., Wei, Q., 2018b. Biosens. Bioelectron. 99, 493–499.

Li, W., Feng, C., Dai, S., Yue, J., Hua, F., Hou, H., 2015. Appl. Catal. B-Environ. 168, 465–471.
Li, X., Wang, Y., Shi, L., Ma, H., Zhang, Y., Du, B., Wu, D., Wei, Q., 2017. Biosens. Bioelectron. 96, 113–120.
Liu, P.P., Liu, X., Huo, X.H., Tang, Y., Xu, J., Ju, H., 2017. ACS Appl. Mater. Inter. 9, 27185–27192.
Liu, Y., Ma, H., Zhang, Y., Pang, X., Fan, D., Wu, D., Wei, Q., 2016. Biosens. Bioelectron. 86, 439–445.
Liu, Y., Zhang, P., Tian, B., Zhang, J., 2015. ACS Appl. Mater. Inter. 7, 13849–13858.
Moualkia, H., Rekhila, G., Mahdjoub, A., Trari, M., 2017. Mater. Sci.-Mater. El. 28, 19105–19112.
Niu, M., Huang, F., Cui, L., Huang, P., Yu, Y., Wang, Y., 2010. ACS Nano 4, 681–688.
Pan, J., Li, J., Yan, Z., Zhou, B., Wu, H., Xiong, X., 2013. Nanoscale 5, 3022–3029.
Ren, X., Ma, H., Zhang, T., Zhang, Y., Yan, T., Du, B., Wei, Q., 2017. ACS Appl. Mater. Inter. 9, 37637–37644.
Shangguan, L., Zhu, W., Xue, Y., Liu, S., 2015. Biosens. Bioelectron. 64, 611–617.
Sheridan, M.V., Hill, D.J., Sherman, B.D., Wang, D., Marquard, S.L., Wee, K.-R., Cahoon, J.F., Meyer, T.J., 2017. Nano Lett. 17, 2440–2446.
Shi, X.-M., Fan, G.-C., Tang, X., Shen, Q., Zhu, J.-J., 2018. Biosens. Bioelectron. 109, 190–196.
Stranick, M.A., Moskwa, A., 1993. Surf. Sci. Spectra 2, 50–54.
Tkachenko, O.P., Shpiro, E.S., Wark, M., Schulz-Ekloff, G., Jaeger, N.I., 1993. J. Chem. Soc. Faraday Trans. 89, 3987–3994.
Vidyasagar, D., Ghugal, S.G., Kulkarni, A., Shende, A.G., Umare, S.S., Sasikala, R., 2018. New J. Chem. 42, 6322–6331.
Wang, J.-X., Zhuo, Y., Zhou, Y., Wang, H.-J., Yuan, R., Chai, Y.-Q., 2016. ACS Appl. Mater. Inter. 8, 12968–12975.
Wang, X., Xu, R., Sun, X., Wang, Y., Ren, X., Du, B., Wu, D., Wei, Q., 2017a. Biosens. Bioelectron. 96, 239–245.
Wang, Y., Fan, D., Zhao, G., Feng, J., Wei, D., Zhang, N., Cao, W., Du, B., Wei, Q., 2018a. Biosens. Bioelectron. 120, 1–7.
Wang, Y., Ge, S., Zhang, L., Yu, J., Yan, M., Huang, J., 2017b. Biosens. Bioelectron. 89, 859–865.
Wang, Y., Zhao, G., Wang, H., Cao, W., Du, B., Wei, Q., 2018b. Biosens. Bioelectron. 106, 179–185.
Xu, R., Jiang, Y., Xia, L., Zhang, T., Xu, L., Zhang, S., Liu, D., Song, H., 2015. Biosens. Bioelectron. 74, 411–417.
Yang, L., Li, Y., Zhang, Y., Fan, D., Pang, X., Wei, Q., Du, B., 2017a. ACS Appl. Mater. Inter. 9, 35260–35267.
Yang, X., Li, X., Zhang, L., Gong, J., 2017b. Biosens. Bioelectron. 92, 61–67.
Zang, Y., Lei, J., Ju, H., 2017. Biosens. Bioelectron. 96, 8–16.
Zhang, X., Liu, M., Liu, H., Zhang, S., 2014a. Biosens. Bioelectron. 56, 307–312.
Zhang, Y.C., Yao, L., Zhang, G., Dionysiou, D.D., Li, J., Du, X., 2014b. Appl. Catal. B-Environ. 144, 730–738.
Zhang, Z., Gao, C., Wu, Z., Han, W., Wang, Y., Fu, W., Li, X., Xie, E., 2016. Nano Energy 19, 318–327.
Zhang, Z., Liu, K., Bao, Y., Dong, B., 2017. Appl. Catal. B-Environ. 203, 599–606.
Zhao, W.-W., Xu, J.-J., Chen, H.-Y., 2017. Biosens. Bioelectron. 92, 294–304.
Zheng, D., Wang, X., 2015. Appl. Catal. B-Environ. 179, 479–488.